



High-capacity NCNT-encapsulated metal NP catalysts on carbonised loofah with dual-reaction centres over C–M bond bridges for Fenton-like degradation of antibiotics

Xiao Zhang^a, Zhongping Yao^{a,*}, Jiankang Wang^b, Wanqian Guo^c, Xiaohong Wu^{a,*}, Zhaohua Jiang^a

^a School of Chemistry and Chemical Engineering, State Key Laboratory of Urban Water Resource and Environment, Harbin Institute of Technology, Harbin 150001, China

^b College of Materials Science and Engineering, Yangtze Normal University, Chongqing 408100, China

^c School of Environmental Engineering, Harbin Institute of Technology, Harbin 150001, China

ARTICLE INFO

Keywords:

C–M bond bridges
Dual-reaction centres
Fenton-like degradation
Antibiotics
Loofah sponge

ABSTRACT

The intensification of electron transport between the dual-reaction centres in Fenton-like catalyst is demonstrated through the incorporation of carbon-metal (C–M) bond bridges. Herein, nitrogen-doped carbon nanotube-encapsulated Fe₃C (Fe₃C@NCNT) with dual-reaction centres over short C–Fe bond was constructed through DFT calculation, and accordingly a series of NCNTs-encapsulated Fe/Fe₃C, Co, and Mo₂C nanoparticles on carbonised loofah were developed by dynamic thermal impregnation and subsequent pyrolysis process. The resultant catalysts displayed satisfactory degradation properties of antibiotics, in which Fe/Fe₃C@NCNTs-CL-800 achieved norfloxacin (NOR) removal efficiency of 93.8% in 90 min under neutral pH, and presented excellent cycle stability in NOR removal as well as universality in various antibiotic degradation systems. The remarkable degradation performance of heterogeneous Fenton-like catalysts was attributed to enhancing electron transport to electron-rich M centres over short C–M bond bridges. This study will open a new perspective on the rational design of catalysts for Fenton-like degradation.

1. Introduction

Currently, the design and development of novel catalysts play key roles in solving energy and environmental problems and strengthening ecological restoration [1–4]. The excessive emission of antibiotics has become a significant problem in the water environment [5–8]. Although heterogeneous Fenton-like technology presents promising advantages in dealing with this issue, the rate-limiting step of the oxidised state ($M^{(n+1)+}$) to the reduced state (M^{n+}) of the metal challenges heterogeneous Fenton-like catalysts [9,10]. Some advances in accelerating electron transfer in the heterogeneous Fenton-like process have been recently achieved, such as using light, electrical, or ultrasound assistance to excite electrons [11–15], adding organic reducing substances to provide electrons [6,16–18], and regulating the electronic structure of catalysts to enhance electron utilization [19–22]. Among them, the construction of dual-reaction centres that consist of an electron-rich reaction region and an electron-poor centre is becoming a vital

method to regulate the electronic structure of catalysts [23–25].

Typically, the electron-rich centre supplies electrons to the activation of hydrogen peroxide, while the electron-poor centre acts as an electron acceptor to receive contaminant electrons and compensate them to the electron-rich centre through transmission channels; in this way, electron transfer and cycling are accomplished. Panjwani et al. reported a novel dual-reaction-centred Fe–Mn–SiO₂ catalyst in which H₂O₂ reduction was achieved on the electron-rich centre around Fe, and electron transfer occurred from the electron-poor centre around Mn to Fe by the Fe–O–Mn bond bridge [25]. Xu et al. designed a Fenton-like Cu–Al₂O₃–g-C₃N₄ catalyst with an electron-rich Cu centre and electron-deficient π -electrons conjugated through a C–O–Cu cross-linker which significantly enhanced electron transfer to promote selective H₂O₂ conversion to \bullet OH [26]. Our previous work also explored the formation of electron-rich Fe centres and electron-poor C centres under the interaction of C–O–Fe bond coupling [27]. These influential studies have greatly spurred the progress of dual-reaction-centred Fenton-like

* Corresponding authors.

E-mail addresses: yaozhongping@hit.edu.cn (Z. Yao), wuxiaohong@hit.edu.cn (X. Wu).

<https://doi.org/10.1016/j.apcatb.2022.121205>

Received 11 September 2021; Received in revised form 7 February 2022; Accepted 9 February 2022

Available online 11 February 2022

0926-3373/© 2022 Elsevier B.V. All rights reserved.

catalysts due to the favourable electron transport channels derived from the interaction between material components.

However, due to the long transfer distance and the transmission resistance from various vibrations or rotations of the chemical bonds, the electron transfer between two atoms is more efficient and easily realised than that among multiple atoms. Therefore, we propose a new strategy of short C–M bonds as electron transport channels between the dual reaction centres for Fenton-like processes. By using the nitrogen-doped carbon nanotube (NCNT) embedded with the Fe_3C cluster over the C–Fe bond ($\text{Fe}_3\text{C}@ \text{NCNT}$) and norfloxacin adsorbed on its surface for configuration optimisation and DFT calculations, dual reaction centres over a short C–Fe bond are constructed. The replenishment of electrons from the adsorbed norfloxacin to the Fe centres during the Fenton-like reaction is indicated.

Based on theoretical analysis, one-dimensional nitrogen-doped carbon nanotubes encapsulating Fe/ Fe_3C nanoparticles on the surface of carbonised loofah ($\text{Fe}/\text{Fe}_3\text{C}@ \text{NCNTs-CL}$) were fabricated through the dynamic thermal impregnation of loofah and $\text{FeCl}_3 \cdot 6 \text{H}_2\text{O}$, followed by direct pyrolysis of the mixture and melamine in an inert atmosphere. NCNT was used to alter the electronic properties and improve the electron fluidity of the carbon matrix for electron-deficient C centres [25,28–30]. Loofah sponge biomass with a unique vascular bundle structure and abundant functional groups was selected as an ideal template to reduce the agglomeration effect of iron nanoparticles (Fe NPs) and improve the loading capacity of Fe NPs inside NCNTs. In the same way, $\text{Co}@ \text{NCNTs-CL}$ and $\text{Mo}_2\text{C}@ \text{NCNTs-CL}$ were successfully synthesised. The as-synthesised materials demonstrate remarkable degradation performance under neutral pH on various antibiotics in the Fenton-like reaction. This work indicates that dual-reaction-centre catalysts over short C–M bond bridges are promising candidates as heterogeneous Fenton-like catalysts for water remediation and opens up a new perspective to design potential catalysts.

2. Computational and experimental sections

2.1. Computational methods

The Vienna Ab initio Simulation Package (VASP) performed all the calculations [31,32]. The interaction between valence electrons and core ions was described by the projector augmented wave (PAW) method [33,34]. The General Gradient Approximation (GGA) with the Perdew, Burke and Ernzerhof (PBE) functional was used to treat the electronic exchange-correlation interactions [35]. The lattice parameters and the ionic positions were fully relaxed, and the final force and total energy were less than $0.05 \text{ eV } \text{\AA}^{-1}$ and 10^{-4} eV for system optimisations. The plane-wave cut-off energy was set to 520 eV to ensure high accuracy. A (6, 6) carbon nanotube was built in this work. The Monkhorst-Pack scheme k-point sampling was used for integration in the first Brillouin zone, and the separation of the k-point mesh was smaller than 0.03 \AA^{-1} [36]. To avoid the interactions between periodic images, a vacuum space of 30 Å along the a and b directions was set for the nanotube models. These models contained (6, 6) single-walled carbon nanotube (CNT), nitrogen-doped carbon nanotube (NCNT), nitrogen-doped carbon nanotubes embedded with Fe_3C clusters connected by Fe–C bond ($\text{Fe}_3\text{C}@ \text{NCNT}$), and antibiotic molecules adsorbed on the $\text{Fe}_3\text{C}@ \text{NCNT}$ surface ($\text{Fe}_3\text{C}@ \text{NCNT-NOR}$). For the $\text{Fe}_3\text{C}@ \text{NCNT}$ and $\text{Fe}_3\text{C}@ \text{NCNT-NOR}$ calculations, spin polarisation was also accounted for. To better describe the interactions between the adsorbed norfloxacin molecule and the host materials, van der Waals (vdW) correction was included in the $\text{Fe}_3\text{C}@ \text{NCNT-NOR}$ calculations. Specifically, the DFT-D3 correction method of Grimme et al. has been employed to treat vdW interactions [37]. The models built in the simulation are much smaller than those observed in the experiment. Still, these simple geometries can reveal the effect on the electronic structure.

2.2. Experimental methods

2.2.1. Chemicals and materials

Iron (III) chloride hexahydrate ($\text{FeCl}_3 \cdot 6 \text{H}_2\text{O}$), cobaltous nitrate hexahydrate ($\text{Co}(\text{NO}_3)_2 \cdot 6 \text{H}_2\text{O}$), ammonium molybdate tetrahydrate ($(\text{NH}_4)_6\text{Mo}_7\text{O}_{24} \cdot 4 \text{H}_2\text{O}$), potassium hydroxide (KOH), ammonium hydroxide ($\text{NH}_3 \cdot \text{H}_2\text{O}$), melamine ($\text{C}_3\text{H}_6\text{N}_6$), hydrogen peroxide (H_2O_2 , 30 wt%), tert-butyl alcohol (TBA), and benzoquinone (BQ) were supplied by Tianjin Yongsheng Fine Chemical Co., Ltd. China. Norfloxacin ($\text{C}_{16}\text{H}_{18}\text{FN}_3\text{O}_3$, NOR), tetracycline hydrochloride ($\text{C}_{22}\text{H}_{25}\text{ClN}_2\text{O}_8$, TCH), and amoxicillin ($\text{C}_{16}\text{H}_{19}\text{N}_3\text{O}_5\text{S}$, AMX) were purchased from Aladdin Industrial Corporation (Shanghai, China). 5, 5-dimethyl-1-pyrroline-1-oxide ($\text{C}_6\text{H}_{11}\text{NO}$, DMPO) was obtained from Sigma-Aldrich. They were directly used without any purification. The loofah sponge used in this study was collected from Farmers' Market of Henan province in China. Meanwhile, deionized water was used in all experiments.

2.2.2. Synthesis

$\text{Fe}/\text{Fe}_3\text{C}@ \text{NCNTs-CL}$ composites were fabricated through dynamic thermal impregnation and an in situ pyrolysis process. In a typical synthesis, the loofah sponge was washed with water and ethanol several times to remove impurities and then dried and crushed. Then, the loofah sponge was hydrotreated with 1 M KOH solution for 10 h at 160°C to remove fat and enhance the surface area and the content of oxygen-containing functional groups [38–40]. After cooling, the loofah was washed with deionised water several times to a neutral pH and dried. Subsequently, 0.5 g treated loofah was completely immersed in 40 mL 0.05 M $\text{FeCl}_3 \cdot 6 \text{H}_2\text{O}$ solution under stirring in an oil bath at 70°C to ensure that Fe^{3+} could be fully adsorbed on the loofah due to its interaction with the surface functional groups of loofah. After stirring for 2 h, 2 mL of 0.5 M ammonia solution was slowly added to precipitate the adsorbed Fe^{3+} . When the solvent evaporated completely, 3 g melamine was added and mixed with the treated loofah. The obtained solid was calcined at different temperatures (700, 800, and 900°C) with a heating rate of 5°C min^{-1} for 2 h in an N_2 atmosphere. Finally, the as-prepared samples were washed to neutral and dried at 60°C . The final products were denoted as $\text{Fe}/\text{Fe}_3\text{C}@ \text{NCNTs-CL-X}$, where CL and X referred to the carbonised loofah and pyrolysis temperature, respectively. For comparison, the sample without adding loofah sponge annealing at 800°C (denoted as $\text{Fe}/\text{Fe}_3\text{C}@ \text{NCNTs}$) was also prepared. Similarly, $\text{Co}@ \text{NCNTs-CL}$ and $\text{Mo}_2\text{C}@ \text{NCNTs-CL}$ composites were obtained in the same manner as $\text{Fe}/\text{Fe}_3\text{C}@ \text{NCNTs-CL-800}$ by adding Co and Mo in equal molar quantities to Fe, respectively.

2.2.3. Characterization

X-ray diffraction (XRD) patterns were performed on an X-ray powder diffractometer using a $\text{Cu K}\alpha$ radiation ($\lambda = 1.5406 \text{ nm}$). The morphologies were observed via a field emission scanning electron microscope (SEM, Helios NanoLab 600i, America). Transmission electron microscopy (TEM) and high-resolution TEM (HRTEM) images were acquired with a Tecnai F20 instrument. X-ray photoelectron spectroscopy (XPS) analysis was conducted with a PHI 5400 ESCA system using $\text{Mg K}\alpha$ radiation as the source at 1253.6 eV. Fourier transform infrared (FT-IR) spectra were carried out on a Nicolet iS50 infrared spectrometer (ThermoFisher, America). Raman spectroscopic system (Renishaw, In Via) with a 633 nm laser was utilized to record Raman spectra. Thermogravimetric (TG) analysis was recorded on an SDT Q600 thermogravimetric analyzer (TA Instruments) in the temperature range of room temperature to 800°C at a heating rate of $10^\circ\text{C min}^{-1}$ under air atmosphere. The magnetic hysteresis loop was measured by a LakeShore 7404 (LakeShore, America) vibrating sample magnetometer (VSM). The multi N/C 3100 TOC analyzer (Jena, Germany) was used to measure the total organic carbon (TOC). Cyclic voltammetry (CV) measurements were performed in an electrochemical workstation (CHI660D, China) with a three-electrode system equipped with a catalyst-supported glassy carbon electrode acting as the working electrode, Pt acting as the

counter electrode and Ag/AgCl electrode acting as the reference electrode in NOR+H₂O₂ solution. The electrochemical study was carried out at room temperature (25 °C). Electron paramagnetic resonance (EPR, Bruker A200, Germany) was employed to detect radicals.

2.2.4. Procedures and analysis

The degradation of NOR evaluated the catalytic activity of catalysts for activating H₂O₂. All experiments were conducted with 50 mL NOR solution under mechanical stirring in a constant temperature water bath. In a typical run, 0.6 g/L catalysts were added to the 0.063 mmol/L NOR solution at pH= 6.2, adjusted by 0.1 M H₂SO₄ or 0.1 M NaOH before the catalytic reaction. After that, the optimal amount of 9 mmol/L H₂O₂ (wt. 30%) was injected into the mixture to initiate the reaction. The weight ratio between hydrogen peroxide and the theoretical COD of 3.37 times the stoichiometric COD was roughly calculated (shown below in Table S2). At determined intervals, 1 mL of solution was withdrawn with a pipette and filtered with a 0.22 µm filter.

The NOR concentration was analysed by high-performance liquid chromatography (HPLC, Thermo U-3000, Germany) equipped with a C18 column (250 mm × 4.6 mm, 5 µm). The mobile phases were 0.025 M phosphoric acid solution (adjusted pH to 3.0 with trimethylamine) and acetonitrile (87: 13, v/v) with a flow rate of 1.0 mL min⁻¹ at 25 °C and a detection wavelength of 278 nm. The degradation products and intermediates of NOR were identified by liquid chromatography coupled with flight-time mass spectrometry (LC-MS, Agilent, America). The total iron leaching in the system was evaluated by the 1,10-phenanthroline method [41]. After the reaction, the catalyst could be separated by an external magnet and dried at 60 °C.

Free radical quenching experiments were performed utilising TBA and BQ as scavengers. The operation was similar to the above degradation experiment, except for the initial addition of 0.5 mL TBA and 0.5 g BQ to restrain the effects of •OH and •O₂⁻ in the solution. Furthermore, a BMPO-trapped electron paramagnetic resonance (EPR) signal was used to detect free radicals by a Bruker EPR A200 spectrometer at room temperature.

3. Results and discussion

3.1. Thermodynamic analysis of dual reaction centres over a C-Fe bond bridge

It is recognised that the cation-π interactions between metal and aromatic carbon rings contribute to the formation of electron-rich centres around the metal and electron-poor C centres [24,42]. Taking the construction of the C-Fe electron channel as an example, the Fe-π interaction through the linkage of C-Fe could account for the dual-reaction centres of electron-rich Fe centres and electron-poor C centres. The construction and optimisation of geometrical configurations of CNT, NCNT, and Fe₃C@NCNT were implemented by employing VASP with density functional theory (DFT), and the optimised models

with different views are shown in Fig. S1. Furthermore, the modified electronic structures were evaluated by comparing the three systems' projected density of states (PDOS). The electron transfer path was analysed through the change in the Fermi level. According to the result in Fig. 1a, compared with the original CNT (Fig. S2), the Fermi level of NCNT is increased by 0.13 eV, implying that the delocalisation of electrons from N to CNTs enhances π electron density and fluidity. Furthermore, the Fermi level of NCNT embedded with the Fe₃C cluster connected through the C-Fe bridge is significantly elevated from -3.18 eV to -3.09 eV compared to NCNT (Fig. 1b), and the Fe₃C@NCNT system obtains higher electron states near the Fermi level than NCNT. The outcomes illustrate that the charge density of the complex is increased with the introduction of Fe₃C.

To investigate the influence of additional organic matter on the electronic structure of the Fe₃C@NCNT system. In our case, norfloxacin (NOR), as a representative antibiotic organic compound, was designed to be adsorbed on the surface of Fe₃C@NCNT (denoted as Fe₃C@NCNT-NOR). After the construction and optimisation of geometrical configurations, Fig. 2a indicates that the electron-poor centre carbon ring is the adsorption site for antibiotic organic compounds, and the adsorption distance between the carbon ring of Fe₃C@NCNT and the aromatic ring of norfloxacin is approximately 3.5 Å, which proves that the two are adsorbed together by π-π stacking [27,43]. As depicted in Fig. 2b, the Fermi energy level of the system further increases from -3.09 eV to -2.98 eV, illustrating that NOR is thermodynamically situated at a higher energy level, which can supply electrons to the carbon ring of the system.

When the Fe₃C@NCNT complex acts as a Fenton-like catalyst in the reaction, the electron-rich Fe centre, as an active catalytic site, first loses electrons, which react with H₂O₂ to form •OH for the degradation of the adsorbed contaminants. The loss of electrons will cause a drop in energy levels around the formed iron ions, which favours the supplementation of electrons at high energy levels from norfloxacin adsorbed on the Fe₃C@NCNT surface by π-π stacking via the short C-Fe channel to iron species for the following reaction with H₂O₂ to form •OH. Therefore, quick electron transfer and cycling in the degradation path are ensured due to the spatial separation of the active catalytic and adsorption sites. In addition, the coexistence of active catalytic sites and adsorption sites within the Fe₃C@NCNT complex significantly shortens the migration distance of the antibiotics to the active sites. Therefore, both are expected to improve the Fenton-like catalytic performance of Fe₃C@NCNT in the degradation of antibiotics.

3.2. Structural characterization of catalysts

Adhering to the DFT results, catalysts of Fe/Fe₃C@NCNTs-CL, Co@NCNTs-CL and Mo₂C@NCNTs-CL were fabricated through dynamic thermal impregnation and pyrolysis, utilising the superiority of the Loofah sponge. Fig. 3a shows XRD patterns of the different composites. Fe/Fe₃C@NCNTs-CL exhibits characteristic diffraction peaks at

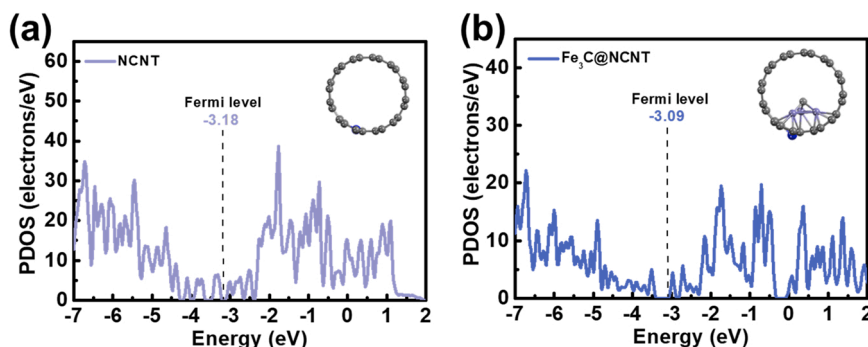


Fig. 1. The projected density of states (PDOS) of (a) NCNT and (b) Fe₃C@NCNT.

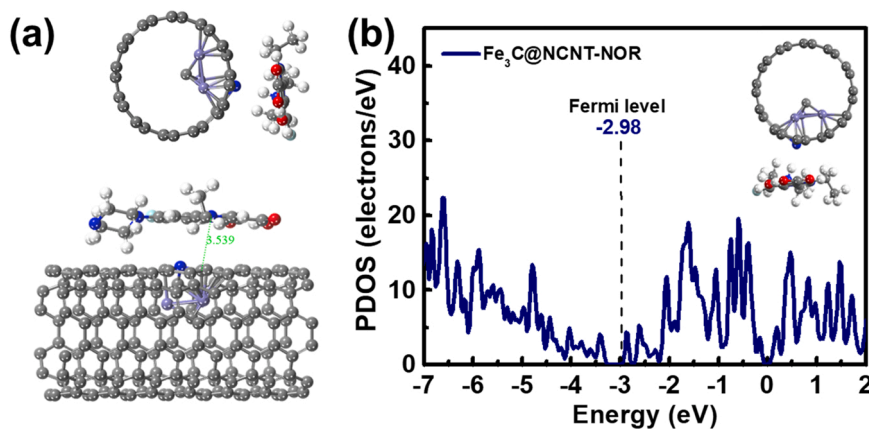


Fig. 2. (a) Model of NOR adsorbed on Fe₃C@NCNT surface and (b) PDOS of Fe₃C@NCNT-NOR.

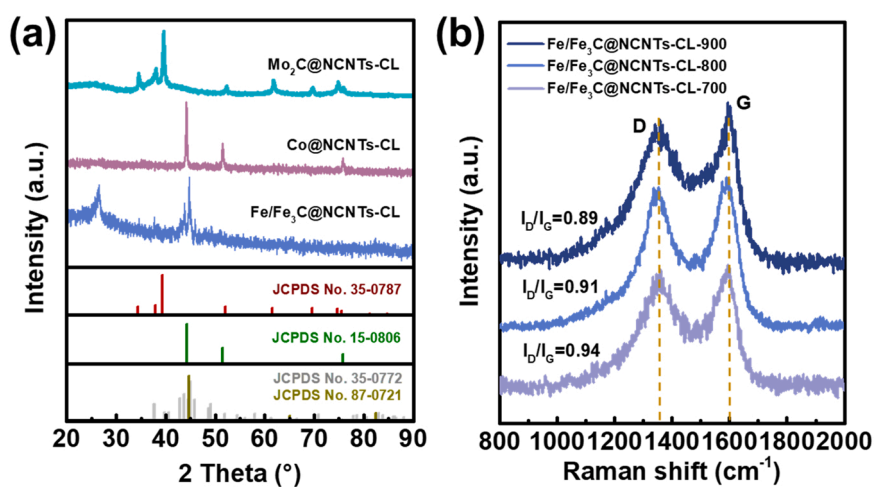


Fig. 3. (a) XRD patterns of different composites and (b) Raman spectra of the Fe/Fe₃C@NCNTs-CL composite at different pyrolysis temperature.

approximately $2\theta = 37.6^\circ, 42.9^\circ, 43.7^\circ, 44.6^\circ, 45.0^\circ, 45.9^\circ$, and 49.1° , which are indexed to the (121), (211), (102), (220), (031), (112), and (221) crystal planes of Fe₃C (JCPDS No. 35-0772), respectively, and the others at approximately $2\theta = 44.7^\circ, 65.0^\circ$, and 82.3° can be associated with the (110), (200), and (211) planes of Fe (JCPDS No. 87-0721). In addition, a sharp peak at approximately $2\theta = 26.5^\circ$ is assigned to the (002) plane of graphitised carbon. In addition, the XRD pattern of Co@NCNTs-CL shows diffraction peaks at $44.2^\circ, 51.5^\circ$, and 75.9° , which are ascribed to Co nanoparticles (JCPDS No. 15-0806). After adding Mo, peaks at $34.4^\circ, 38.0^\circ, 39.4^\circ, 52.1^\circ, 61.5^\circ, 69.6^\circ, 74.6^\circ$, and 75.5° appear corresponding to the (100), (002), (101), (102), (110), (103), (112), and (201) planes of the Mo₂C phase (JCPDS No. 35-0787), respectively. The results indicate that these catalysts were successfully synthesised.

Beyond that, the Fe/Fe₃C@NCNTs-CL material was synthesised at different pyrolysis temperatures. As seen from Fig. S3, Fe/Fe₃C@NCNTs-CL-700, Fe/Fe₃C@NCNTs-CL-800, and Fe/Fe₃C@NCNTs-CL-900 manifest almost identical characteristic diffraction peaks. It is worth noting that the relative contents of Fe/Fe₃C in the three samples reveal an evident elevation with temperatures from 700 °C to 900 °C, indicating that the composition of iron species in the composites can be adjusted by pyrolysis temperature [44]. In addition, the XRD pattern of the contrast sample is exhibited in Fig. S4. The diffraction peaks of Fe/Fe₃C@NCNTs located at approximately $43.7^\circ, 44.6^\circ$, and 45.0° are attributed to the (102), (220), and (031) crystalline planes of Fe₃C, along with the strong diffraction peaks at approximately $2\theta = 44.7^\circ$, indicating the presence of Fe.

To identify the graphitisation degree of the carbon component in the

composites, Raman spectra of Fe/Fe₃C@NCNTs-CL-700, Fe/Fe₃C@NCNTs-CL-800, and Fe/Fe₃C@NCNTs-CL-900 are exhibited in Fig. 3b. Three samples display similar spectra with two distinguishable peaks corresponding to the D-band and G-band at approximately 1350 and 1580 cm⁻¹, respectively. The G-band refers to the stretching of carbon atoms with sp² hybridisation. The D-band derives from disordered carbon; thus, the intensity ratio of the D-band to the G-band (I_D/I_G) is employed to evaluate the change in graphitisation degree. It is clear that the I_D/I_G value gradually decreases from 0.96 (Fe/Fe₃C@NCNTs-CL-700) to 0.82 (Fe/Fe₃C@NCNTs-CL-900), implying that the graphitisation degree of the carbon component in these composites is improved as the pyrolysis temperature increases from 700 °C to 900 °C. In general, a graphite structure is beneficial for improving the charge transfer process [45]; therefore, carbon materials with a high graphitisation degree promote electron transfer between H₂O₂ and the catalyst, thus speeding up the Fenton-like catalytic reaction rate.

SEM images untangle the microstructure of Fe/Fe₃C@NCNTs-CL, Co@NCNTs-CL, and Mo₂C@NCNTs-CL in Fig. 4a-c, and all of them feature a structure with a dispersed NCNTs framework on the loofah. There is a consensus that the decomposition product of melamine is deposited on the surface of iron, cobalt, and molybdenum nanoparticles, which catalyse the recrystallisation of carbon to form NCNTs [46-50]. The preparation of materials is closely related to the process conditions. In particular, Fe/Fe₃C@NCNTs-CL was selected as the key research target.

Generally, the proportion of raw materials will affect the morphology of the final composite. As shown in Fig. S5, we modulated

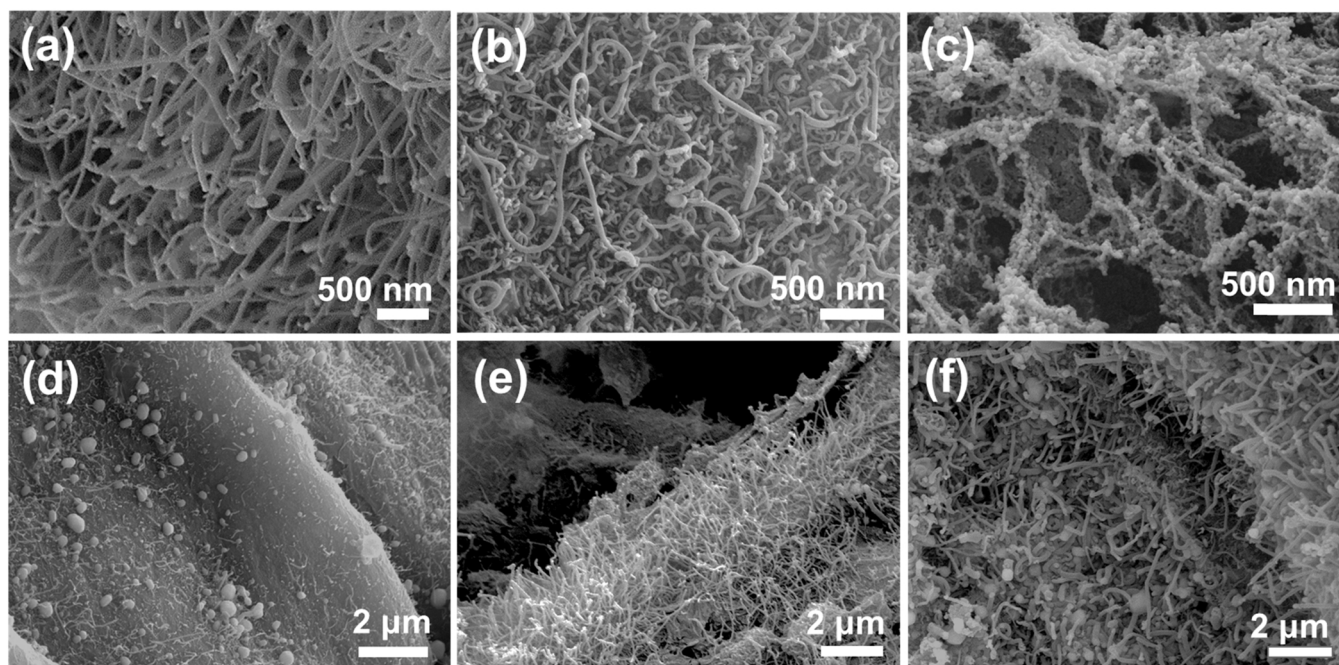


Fig. 4. SEM images of (a) Fe/Fe₃C@NCNTs-CL, (b) Co@NCNTs-CL, (c) Mo₂C@NCNTs-CL, (d) Fe/Fe₃C@NCNTs-CL-700, (e) Fe/Fe₃C@NCNTs-CL-800, and (f) Fe/Fe₃C@NCNTs-CL-900.

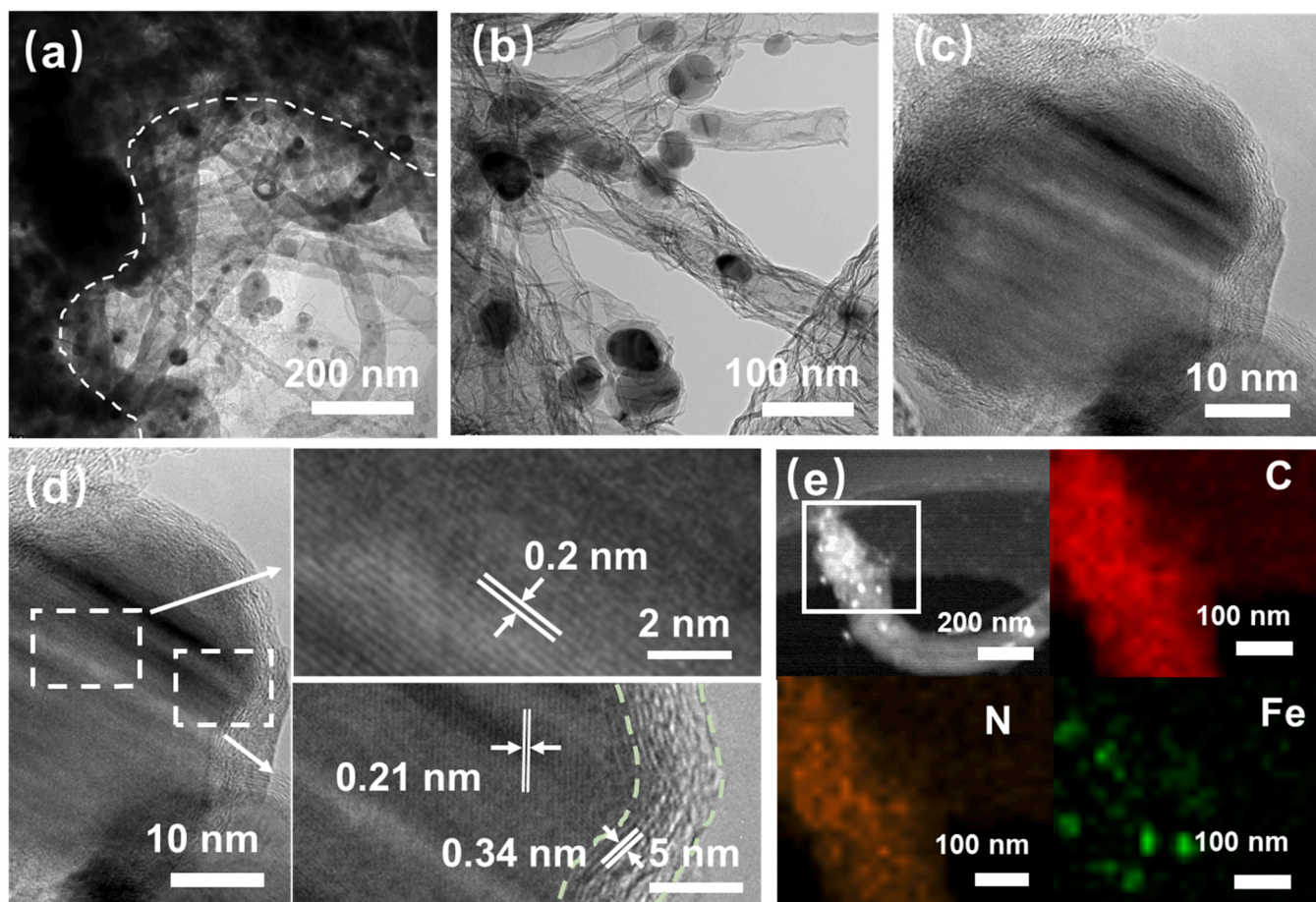


Fig. 5. TEM images of (a, b) Fe/Fe₃C@NCNTs-CL-800, (c, d) HRTEM images of Fe/Fe₃C@NCNTs-CL-800, and (e) EDS elemental mappings (C, N and Fe) of Fe/Fe₃C@NCNTs-CL-800.

the weight ratio of melamine and $\text{FeCl}_3 \cdot 6\text{H}_2\text{O}$ from 1:0.05, 1:0.17, to 1:0.33 in the composite, denoted $\text{Fe}/\text{Fe}_3\text{C}@\text{NCNTs-CL-}\#1$, $\text{Fe}/\text{Fe}_3\text{C}@\text{NCNTs-CL-}\#2$, and $\text{Fe}/\text{Fe}_3\text{C}@\text{NCNTs-CL-}\#3$, respectively. When the iron source is insufficient (Fig. S5a), the complete conversion of melamine into NCNTs cannot be realised, resulting in a large number of disordered carbon species covering the loofah surface. If the iron source is excessive (Fig. S5c), then Fe particles agglomerate severely outside the NCNTs because not enough NCNTs are generated to hold all Fe particles. As observed in Fig. S5b, only under the suitable proportion of melamine and $\text{FeCl}_3 \cdot 6\text{H}_2\text{O}$ does the optimal morphology appear to be well encapsulated in NCNTs. Therefore, the appropriate weight ratio of melamine and $\text{FeCl}_3 \cdot 6\text{H}_2\text{O}$ at 1:0.17 was selected in this work.

In addition, the morphologies of samples at three pyrolysis temperatures were studied in depth. The as-prepared $\text{Fe}/\text{Fe}_3\text{C}@\text{NCNTs-CL-700}$, $\text{Fe}/\text{Fe}_3\text{C}@\text{NCNTs-CL-800}$, and $\text{Fe}/\text{Fe}_3\text{C}@\text{NCNTs-CL-900}$ all present unique one-dimensional microstructures supported by biomorphic carbon of loofah. At 700 °C (Fig. 4d), one-dimensional nanotubes of the sample just appeared under the catalysis of Fe NPs, and an incomplete tube structure was formed with a diameter of only 40–60 nm. $\text{Fe}/\text{Fe}_3\text{C}@\text{NCNTs-CL-800}$ presents uniform and regularly arranged nanotubes with a diameter range of 80–120 nm, which combine to the loofah surface neatly (Fig. 4e). When the pyrolysis temperature reaches 900 °C, Fig. 4f shows that the diameters of the tubes further increase to 160–200 nm, but the collapse and damage of nanotubes occur due to the high temperature. Therefore, at 800 °C, an intact tube structure was obtained with the proper graphitisation degree, ensuring Fe's effective loading and improved charge transfer for the Fenton-like process.

A typical view of $\text{Fe}/\text{Fe}_3\text{C}@\text{NCNTs-CL-800}$ (Fig. S6) shows that the obtained sample inherits the porous channel morphology of the loofah well, and the surface is densely and orderly coated with nanotubes. In contrast, the synthesised $\text{Fe}/\text{Fe}_3\text{C}@\text{NCNTs}$ (Fig. S7) show evident agglomeration and the rupture of NCNTs, and iron particles accumulate heavily outside the tubes because iron nanoparticles are not well wrapped by NCNTs, indicating that loofah could act as an ideal carrier for dispersing iron species by further providing sites to induce the growth of NCNTs and prevent their aggregation and rupture.

Furthermore, TEM images of $\text{Fe}/\text{Fe}_3\text{C}@\text{NCNTs-CL-800}$ were obtained to understand its microstructure fully. As confirmed in Fig. 5a, NCNTs are grown on the loofah surface, where the dotted lines represent

the binding surface of the two substances. A close inspection of NCNTS (Fig. 5b) confirms that Fe NPs with a particle size of approximately 50 nm are encapsulated in intact nanotubes. The HRTEM image reveals that the core-shell structure with well-ordered carbon shells is arranged around the Fe NPs (Fig. 5c). Additionally, as shown in Fig. 5d, the outside part with a lattice spacing of 0.34 nm is ascribed to the (002) plane of graphite carbon. The inner lattice fringes of nanoparticles are 0.20 and 0.21 nm, corresponding to the (110) face of Fe and the (211) face of Fe_3C , suggesting that the iron core should be a mixture of Fe surrounded by Fe_3C . The growth mechanism can be explained by the fact that an adequately high pyrolysis temperature is favourable for melamine decomposition and reducing iron species to metallic Fe. Then the carbon species are captured by Fe nanoparticles to form a graphite carbon layer, accompanied by a carburising reaction between iron atoms and adjacent carbon atoms to generate Fe_3C [46,51]. The unique configuration is believed to be helpful to prevent iron leaching and oxidation. The EDS elemental mapping (Fig. 5e) results also support the distribution of C and N elements in the carbon tubes. At the same time, Fe only appears inside the tube, implying that N is successfully doped into the CNT, and $\text{Fe}/\text{Fe}_3\text{C}$ nanoparticles are encapsulated in NCNTs and bonded by a C–Fe bridge.

XPS further characterised the chemical composition and bonding state of $\text{Fe}/\text{Fe}_3\text{C}@\text{NCNTs-CL-800}$. The survey spectra reveal the presence of C, N, O, and Fe (Fig. 6a). The weak signal of Fe was attributed to most of the Fe-related nanoparticles being coated with the carbon shell and unable to be effectively analysed. Furthermore, the Fe content of the composite was revealed through TGA analysis. As illustrated in Fig. S8, the sample undergoes a negligible weight loss between 25 and 300 °C, mainly attributed to the evaporation of adsorbed water. The curve declines sharply at 300–500 °C due to the combustion of carbon. Ultimately, the complete combustion of the carbon and total oxidation of $\text{Fe}/\text{Fe}_3\text{C}$ nanoparticles at 500 °C resulted in only Fe_2O_3 as the final product, and the residual was 29.63%. Thus, the calculated iron content is approximately 20.74%. The C 1s spectra are divided into five peaks, as displayed in Fig. 6b. Among them, the peaks located at 284.6 eV, 286.5 eV, and 288.6 eV are in accordance with C=C, C–O, and –COOH, respectively [52,53]. In addition, the peak at 285.6 eV corresponds to C–N, suggesting that N atoms are successfully incorporated into the carbon structure [54], and the peak at approximately 283.6 eV indicates

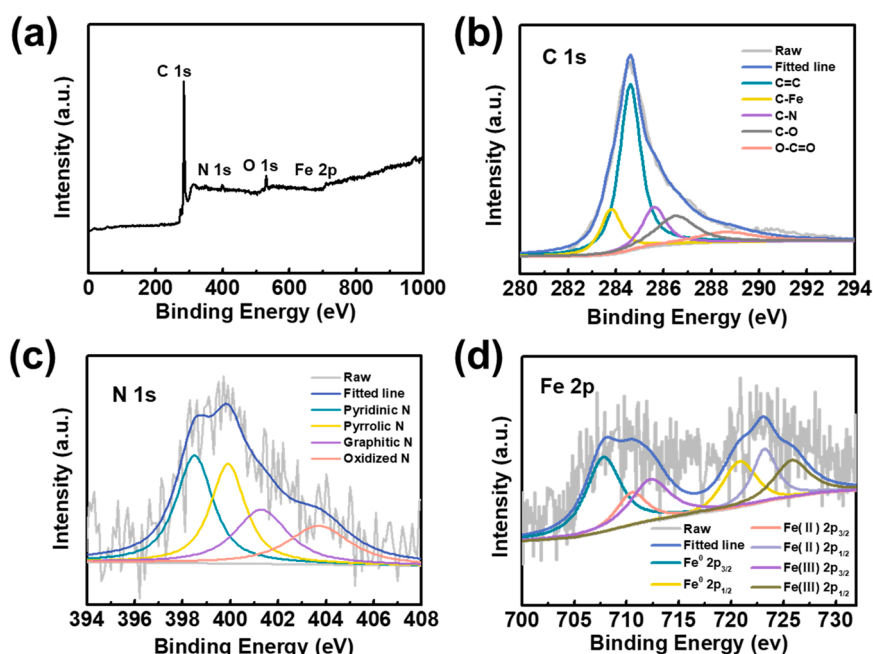


Fig. 6. XPS spectra of $\text{Fe}/\text{Fe}_3\text{C}@\text{NCNTs-CL-800}$: (a) wide scan, (b) C1s, (c) N1s and (d) Fe2p.

C–Fe bonds that come from Fe_3C and further demonstrates that Fe–C interactions connect Fe NPs and NCNTs [55]. The N 1s spectra can be classified into pyridinic, pyrrolic, graphitic, and oxidised N with binding energies of 398.5 eV, 399.8 eV, 401.3 eV, and 403.7 eV, respectively (Fig. 6c) [56]. It is generally believed that the doped nitrogen atoms in the graphitic layer can alter the electronic structure of the original carbon skeleton to produce more defects, accelerate electron transfer, and enhance catalytic performance [57,58]. The high-resolution Fe 2p spectra (Fig. 6d) are divided into six peaks, where 707.8 eV and 720.8 eV are assigned to Fe^0 2p_{3/2} and Fe^0 2p_{1/2}, respectively. Moreover, the peaks at 710.5 eV and 723.2 eV correspond to Fe(II) 2p_{3/2} and Fe(II) 2p_{1/2}, and the binding energies at 712.3 eV and 725.8 eV are attributed to Fe(III) 2p_{3/2} and Fe(III) 2p_{1/2}, which might result from the inevitable oxidation of the surface [59,60]. The surface functional groups of $\text{Fe/Fe}_3\text{C@NCNTs-CL-800}$ were further investigated by FTIR (Fig. 7a). The band at approximately 3421 cm^{-1} is ascribed to O–H stretching vibrations. The characteristic peak at approximately 1626 cm^{-1} is assigned to C=C [61,62]. The peaks at 1386 cm^{-1} and 1092 cm^{-1} are characteristic of the C–N and C–O vibrations, respectively [63,64]. Furthermore, the appearance of a C–Fe bond at 603 cm^{-1} again proves the possibility of a C–Fe linkage between Fe and NCNTs and the presence of Fe_3C [56].

Moreover, to investigate the electrochemical properties of $\text{Fe/Fe}_3\text{C@NCNTs-CL-800}$, the cyclic voltammetry (CV) curves of $\text{Fe/Fe}_3\text{C@NCNTs-CL-800}$ compared with those of $\text{Fe/Fe}_3\text{C@NCNTs}$ in the NOR system are presented in Fig. 7b. $\text{Fe/Fe}_3\text{C@NCNTs-CL-800}$ exhibits a narrower CV size than $\text{Fe/Fe}_3\text{C@NCNTs}$, which indicates that the electron transfer efficiency is accelerated upon introduction of the loofah sponge carrier [65]. In addition, two significant peaks of oxidation current (I_{pa}) at 0.191 V and reduction current (I_{pc}) at 0.118 V are present in the $\text{Fe/Fe}_3\text{C@NCNTs-CL-800}$ curve with a higher current density, implying the existence of an $\text{Fe}^{\text{III}}/\text{Fe}^{\text{II}}$ redox reaction at the catalyst interface in the NOR system. Simultaneously, the CV curve represents an excellent reversible process as the ratio of I_{pc} to I_{pa} is close to 1. The potential separation ΔE ($E_{\text{pa}} - E_{\text{pc}}$) is approximately 73 mV [66,67], which is lower than $\text{Fe/Fe}_3\text{C@NCNTs}$ (179 mV). These results demonstrate that $\text{Fe/Fe}_3\text{C@NCNTs-CL-800}$ requires less driving force for the redox reaction, which is thermodynamically favourable for electron transfer. The excellent $\text{Fe}^{\text{III}}/\text{Fe}^{\text{II}}$ redox cycle of $\text{Fe/Fe}_3\text{C@NCNTs-CL-800}$ may be attributed to $\text{Fe/Fe}_3\text{C}$ being encapsulated in NCNTs via C–Fe bonds, facilitating electron transfer to Fe species. This result is consistent with the expected theoretical calculations.

In brief, $\text{Fe/Fe}_3\text{C}$ encapsulated in NCNTs supported by loofah was successfully synthesised. As a carrier, the loofah sponge could improve the dispersion of active component nanotubes, which promotes electron transfer from NCNTs to Fe NPs based on the C–Fe connection between them, generating an electron-rich Fe centre to decompose H_2O_2 efficiently. According to the DFT calculation results, this will give $\text{Fe/Fe}_3\text{C@NCNTs-CL-800}$ remarkable Fenton-like catalytic performance.

3.3. Catalytic performance of catalysts

The degradation effect of NOR evaluated the catalytic performances of the as-obtained catalysts for H_2O_2 activation. To determine the optimal degradation conditions, the influence of initial pH, catalyst dosage, H_2O_2 dosage, and temperature on NOR conversion with $\text{Fe/Fe}_3\text{C@NCNTs-CL-800}$ was further evaluated, as shown in Fig. S9. At the outset, $\text{Fe/Fe}_3\text{C@NCNTs-CL}$, Co@NCNTs-CL , and $\text{Mo}_2\text{C@NCNTs-CL}$ were added to the reaction solution to differentiate the removal effect of NOR by physical adsorption. As a result, only 23.1%, 25.2%, and 19.7% NOR removal could be achieved within 40 min (Fig. S10), meaning that the adsorption capacity of the catalyst is limited. However, the degradation efficiencies of NOR are dramatically improved under the coexistence of H_2O_2 and catalyst (Fig. 8a). Specifically, NOR conversion with $\text{Fe/Fe}_3\text{C@NCNTs-CL}$, Co@NCNTs-CL , and $\text{Mo}_2\text{C@NCNTs-CL}$ can reach 93.8%, 92.1%, and 88.4%, respectively, within 90 min. These results indicate that NOR is removed simultaneously through adsorption and degradation in the early stage. When the adsorption reaches equilibrium, the degradation process dominates the removal of NOR.

In particular, a detailed study on the effect of the carrier (loofah) and pyrolysis temperature on the catalytic performance was carried out for $\text{Fe/Fe}_3\text{C@NCNTs-CL}$. In Fig. S11, it can be observed that $\text{Fe/Fe}_3\text{C@NCNTs-CL-800}$ yields an optimal degradation efficiency of 93.8% within 90 min. For comparison, $\text{Fe/Fe}_3\text{C@NCNTs}$, $\text{Fe/Fe}_3\text{C@NCNTs-CL-700}$, and $\text{Fe/Fe}_3\text{C@NCNTs-CL-900}$ display relatively inferior catalytic efficiencies of 68.9%, 77.3%, and 88.1%, respectively, for NOR conversion within 90 min. For comprehensive consideration, loofah as a carrier can disperse the growth of NCNTs well to improve the catalytic activity. However, the carbon tubes at a low temperature of 700 °C are not fully formed, and the graphitisation degree is relatively low, leading to unsatisfactory catalytic performance. A high annealing temperature of 800 °C will cause aggregation and damage of NCNTs, leading to a decline in catalyst activity. Accordingly, it can be inferred that the outstanding catalytic performance of $\text{Fe/Fe}_3\text{C@NCNTs-CL-800}$ benefits from establishing an efficient electron transport structure, where Fe NPs are uniformly embedded in integrated nanotubes with favourable dispersion through the C–Fe link. To further highlight the superiority of $\text{Fe/Fe}_3\text{C@NCNTs-CL-800}$, the kinetic curves for NOR degradation by various catalysts are fitted with the quasi-first order equation in Fig. 8b. The reaction rate constants of $\text{Fe/Fe}_3\text{C@NCNTs-CL-800}$ ($k = 0.0275 \text{ min}^{-1}$) are 2.5 times higher than those of $\text{Fe/Fe}_3\text{C@NCNTs}$ ($k = 0.0109 \text{ min}^{-1}$) and 1.3 and 1.8 times higher than those of $\text{Fe/Fe}_3\text{C@NCNTs-CL-700}$ ($k = 0.0214 \text{ min}^{-1}$) and $\text{Fe/Fe}_3\text{C@NCNTs-CL-900}$ ($k = 0.0154 \text{ min}^{-1}$), respectively. A deeper TOC test shows that approximately 68.26% of TOC is removed using $\text{Fe/Fe}_3\text{C@NCNTs-CL-800}$ as the Fenton-like catalyst to degrade NOR within 90 min. The corresponding TOC data are provided in Table S1. The HPLC chromatogram of NOR degradation by $\text{Fe/Fe}_3\text{C@NCNTs-CL-800}$ is depicted in Fig. 8c. The corresponding parent peak appears at approximately 10.7 min and decreases gradually or even nearly disappears with the extension of the Fenton-like degradation time.

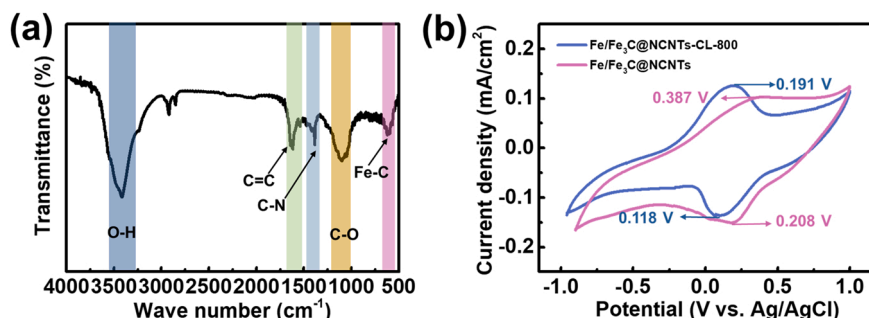


Fig. 7. (a) FTIR spectrum of $\text{Fe/Fe}_3\text{C@NCNTs-CL-800}$ and (b) cyclic voltammetry curves of $\text{Fe/Fe}_3\text{C@NCNTs-CL-800}$ and $\text{Fe/Fe}_3\text{C@NCNTs}$.

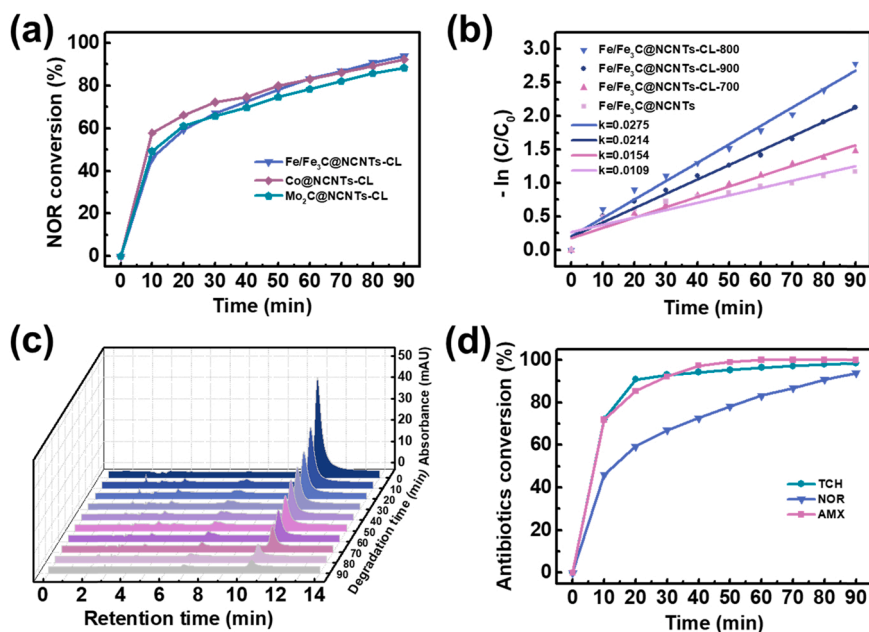


Fig. 8. (a) NOR conversion under the coexistence of H₂O₂ and catalysts, (b) kinetic curves for NOR removal by Fe/Fe₃C@NCNTs-CL-X, (c) HPLC chromatogram of NOR conversion with Fe/Fe₃C@NCNTs-CL-800, and (d) degradation of various antibiotics by Fe/Fe₃C@NCNTs-CL-800. Reaction conditions: [NOR] = 0.063 mmol/L, [TCH] = 0.073 mmol/L, [AMX] = 0.083 mmol/L, [catalyst] = 0.6 g/L, [H₂O₂] = 9 mmol/L, pH = 6.2, and T = 303.15 K.

To demonstrate the universal applicability of the catalyst, Fe/Fe₃C@NCNTs-CL-800 was also used for the degradation of other representative antibiotics, including tetracycline hydrochloride (TCH) and amoxicillin (AMX), in addition to NOR. In Fig. 8d, the degradation efficiency of TCH reaches 98.5%, which exhibits a more significant advantage than the catalyst over the C–O–Fe bond in our previous work [27], as shown in Fig. S12, and AMX can be almost completely removed within 90 min, indicating that Fe/Fe₃C@NCNTs-CL-800 with such a structure of dual-reaction centres over short C–Fe bonds is indeed an excellent heterogeneous Fenton-like catalyst for the treatment of wastewater containing different antibiotic pollutants. Following this, Co@NCNTs-CL and Mo₂C@NCNTs-CL catalysts prepared in the same

way in this work both have excellent performance due to the short C–M electron transport channel.

In short, these results confirm that the as-prepared Fe/Fe₃C@NCNTs-CL-800 with a C–Fe bond bridge structure displays remarkable Fenton-like catalytic performance under circumneutral pH, which presents apparent advantages among the other Fenton-like catalysts used for NOR removal listed in Table S2.

The stability of the catalyst is another important aspect to be considered in practical applications, and five cycle tests were carried out under the same conditions (Fig. 9a). Compared with 93.8% NOR removal in the first run, the degradation rate was reduced to 83.9% after five runs. The slight performance degradation of Fe/Fe₃C@NCNTs-CL-

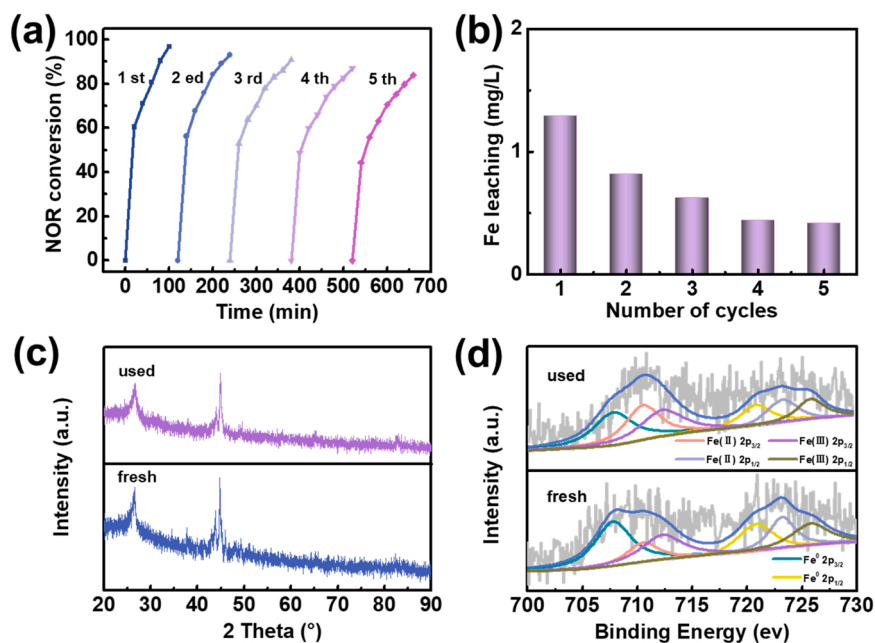


Fig. 9. (a) Evaluation of the stability of Fe/Fe₃C@NCNTs-CL-800, (b) iron leaching amount in five cycles, (c) XRD patterns of fresh and used Fe/Fe₃C@NCNTs-CL-800, and (d) Fe 2p XPS spectra of fresh and used Fe/Fe₃C@NCNTs-CL-800.

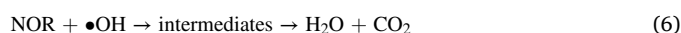
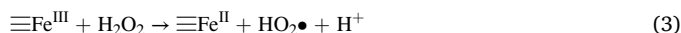
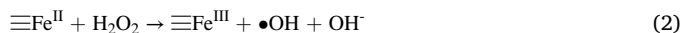
800 resulted from the inevitable loss of catalyst and iron leaching during the cycle. Furthermore, after using Fe/Fe₃C@NCNTs-CL-800, the Fe leaching amount in the reaction solution decreased from 1.29 mg/L to 0.42 mg/L (Fig. 9b), validating that the structure of Fe nanoparticles embedded in nitrogen-doped carbon nanotubes is stable and has excellent cycling stability. In the meantime, the magnetic properties of the catalyst were characterised by a hysteresis curve at room temperature. As indicated in Fig. S13, the saturation magnetisation (M_s) value is 42.3 emu g⁻¹, which suggests that an external magnetic field can easily separate the catalyst for reuse. To further explore the stability of Fe/Fe₃C@NCNTs-CL-800, the XRD patterns of samples before reaction (fresh) and after five cycles (used) are displayed in Fig. 9c. There is no significant change in the characteristic peak except for a slight decrease in the relative amount of Fe₃C after reaction, indicating that the active sites of iron species are comparatively stable in the Fe/Fe₃C@NCNTs-CL-800/H₂O₂ system. In Fig. S14, the SEM image of Fe/Fe₃C@NCNTs-CL-800 after 5 cycles reveals that the catalyst still maintains a relatively intact and ordered tubular structure, illustrating that such a structure prevented the iron species from losing and destroying. Moreover, XPS spectra reveal the variation in valence states of the active species before and after the reaction. As seen from Fig. 9d, the $\equiv\text{Fe}^0$ content in the used catalyst decreases because of the reaction of Fe₃C with H₂O₂, whereas the $\equiv\text{Fe}^{\text{II}}$ content increases and accounts for the most significant proportion. The main reasons may be that, on the one hand, $\equiv\text{Fe}^{\text{III}}$ generated from Fe₃C in the outer layer is normalised with Fe in the core to form $\equiv\text{Fe}^{\text{II}}$. On the other hand, the catalyst will receive electrons from NOR to reduce $\equiv\text{Fe}^{\text{III}}$ to $\equiv\text{Fe}^{\text{II}}$, ensuring the high catalytic activity of Fe/Fe₃C@NCNTs-CL-800. Given this, the as-prepared Fe/Fe₃C@NCNTs-CL-800 is a satisfactory heterogeneous catalyst with good stability and repeatability for the disposal of antibiotic wastewater.

3.4. Catalytic mechanism analysis

H₂O₂ can be activated in the Fenton reaction to produce reactive oxygen species (ROS), generally referred to as $\bullet\text{OH}$ and $\bullet\text{O}_2^-$ to oxidise contaminants. To discriminate the types of ROS and their contribution to the reaction in the Fe/Fe₃C@NCNTs-CL-800/H₂O₂ system, free radical quenching experiments were conducted with different scavenging agents (Fig. 10a). TBA and BQ, as scavengers, were selected to verify the existence of $\bullet\text{OH}$ and $\bullet\text{O}_2^-$, respectively. Compared with that of the control condition, the NOR conversion is significantly impeded by TBA. Still, the NOR degradation effect is slightly reduced after adding BQ, indicating that $\bullet\text{OH}$ makes a dominant contribution to the degradation process, while $\bullet\text{O}_2^-$ only plays a weak role. To further identify ROS in the Fe/Fe₃C@NCNTs-CL-800/H₂O₂ system, the DMPO-trapped EPR technique was carried out. As shown in Fig. 10b, the EPR signal could not be detected when only H₂O₂ was added, suggesting that H₂O₂ could not self-activate. After adding Fe/Fe₃C@NCNTs-CL-800 and H₂O₂, four characteristic peaks with an intensity ratio of 1:2:2:1 can be found, attributed to the DMPO- $\bullet\text{OH}$ adduct signal. Nevertheless, owing to the small amount of $\bullet\text{O}_2^-$ and its rapid reaction with iron ions [68], the

DMPO- $\bullet\text{O}_2^-$ signal has not been explored, which further certifies that $\bullet\text{OH}$ is the dominant active species for NOR degradation.

Based on these results, a plausible reaction mechanism of Fenton-like degradation of NOR in the Fe/Fe₃C@NCNTs-CL-800/H₂O₂ system is proposed and illustrated in Scheme 1. When Fe/Fe₃C@NCNTs-CL-800 is utilised as a Fenton-like catalyst to activate H₂O₂, $\equiv\text{Fe}^0$ in the outer layer reacts with H₂O₂ to produce $\equiv\text{Fe}^{\text{II}}$ (Eq. 1), which acts as the primary active sites for converting H₂O₂ to $\bullet\text{OH}$ through Eq. 2. Nevertheless, in the classic Fenton-like process, the transformation of $\equiv\text{Fe}^{\text{III}}$ to $\equiv\text{Fe}^{\text{II}}$ is the rate-determining step (Eq. 3); thus, the regeneration of $\equiv\text{Fe}^{\text{II}}$ is accomplished rapidly by Eq. 4 and Eq. 5. Specifically, forming $\equiv\text{Fe}^{\text{III}}$ normalises with the remaining $\equiv\text{Fe}^0$ to yield $\equiv\text{Fe}^{\text{II}}$ via Eq. 4. More importantly, NOR and its intermediates are adsorbed on the NCNTs, and their electrons are delivered to the carbon ring of the nanotubes through π - π stacking, which is then compensated to $\equiv\text{Fe}^{\text{III}}$ by C-Fe channels (Eq. 5), generating electron-rich Fe centres and electron-poor C centres. Moreover, N modification effectively regulates the electronic structure of the carbon skeleton. It accelerates the flow and transmission of π electrons, which leads to the formation of abundant $\equiv\text{Fe}^{\text{II}}$ in favour of facilitating activation of H₂O₂ to produce more $\bullet\text{OH}$. The intermediates were detected by LC-MS analysis, and four possible NOR degradation pathways are proposed in Fig. S15. Ultimately, under the continuous attack of $\bullet\text{OH}$, the intermediates can be mineralised into small molecules such as CO₂, H₂O, F⁻, and NO₃⁻ (Eq. 6), which endows Fe/Fe₃C@NCNTs-CL-800 with prominent Fenton-like catalytic performance and stability.



4. Conclusions

In summary, we proposed the strategy of using short C-M bonds as electron transport channels between the dual-reaction centres for the Fenton-like process. We successfully synthesised a series of catalysts of NCNTs embedded with Fe/Fe₃C, Co, and Mo₂C nanoparticles on a carbonised loofah surface by dynamic thermal impregnation and pyrolysis. The designed structure of NCNT encapsulating Fe₃C clusters over C-Fe bonds forms electron-rich Fe centres and electron-poor C centres. The DFT calculation illustrates that the adsorbed antibiotic of NOR is thermodynamically favourable for supplying electrons to the Fe centre by π - π stacking and the short C-Fe channel. The three as-synthesized Fenton-like catalysts all manifest remarkable degradation performance

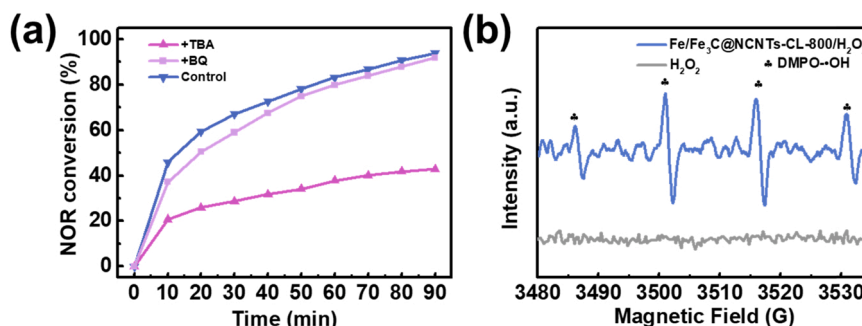
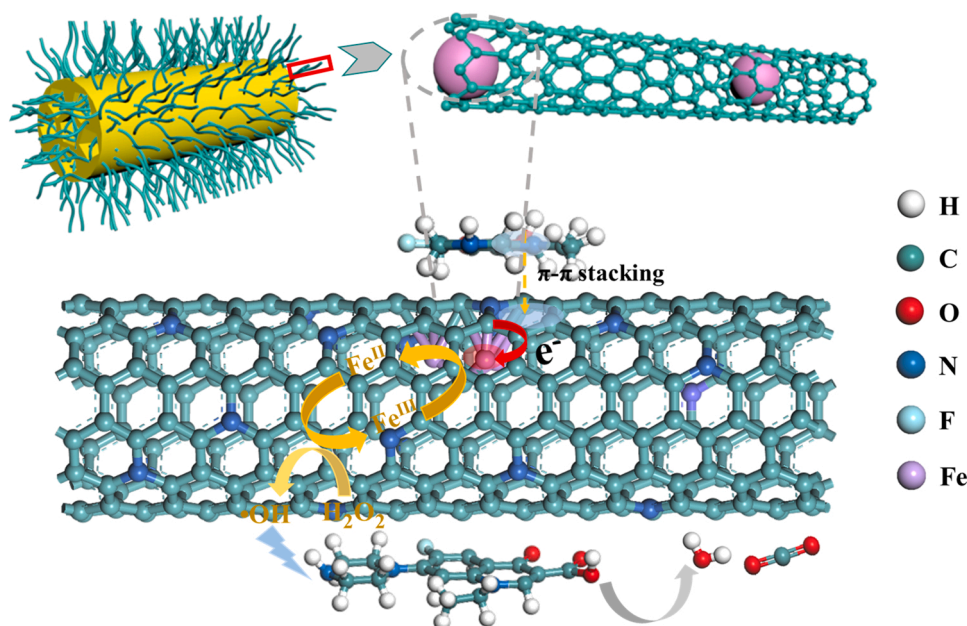


Fig. 10. (a) Effect of radical quenching scavengers on NOR conversion and (b) DMPO-trapped EPR spectra of Fe/Fe₃C@NCNTs-CL-800/H₂O₂ system.



Scheme 1. Plausible reaction mechanism of Fenton-like degradation of NOR in Fe/Fe₃C@NCNTs-CL-800/H₂O₂ system.

on NOR under neutral pH, among which Fe/Fe₃C@NCNTs-CL-800 displays the optimal NOR removal efficiency of 93.8% within 90 min. The universal applicability of Fe/Fe₃C@NCNTs-CL-800 is verified through the rapid degradation of various antibiotics, including NOR, TCH, and AMX, and the removal efficiency of TCH reaches 98.5%. AMX can be almost completely removed within 90 min. In addition, cycle tests show that it possesses excellent stability. This study offers a valuable clue to design high-performance Fenton-like catalysts to treat wastewater containing different antibiotic pollutants.

CRedit authorship contribution statement

Xiao Zhang: Conceptualization, Methodology, Data curation, Writing – original draft, Writing – review & editing, Supervision, Project administration, Software. **Zhongping Yao:** Methodology, Data curation, Writing – review & editing, Supervision, Funding acquisition. **Jiankang Wang:** Data curation, Investigation, Funding acquisition. **Wanqian Guo:** Validation, Supervision. **Xiaohong Wu:** Data curation, Investigation. **Zhaohua Jiang:** Conceptualization, Methodology, Supervision, Funding acquisition.

Declaration of Competing Interest

The authors declare that they have no known competing financial interests or personal relationships that could have appeared to influence the work reported in this paper.

Acknowledgment

This work is supported by National Natural Science Foundation of China (No. 51571076, 21906008), and Open Project of State Key Laboratory of Urban Water Resource and Environment, Harbin Institute of Technology, China (No. HCK202115).

Appendix A. Supporting information

Supplementary data associated with this article can be found in the online version at [doi:10.1016/j.apcatb.2022.121205](https://doi.org/10.1016/j.apcatb.2022.121205).

References

- [1] L.C. Seitz, C.F. Dickens, K. Nishio, Y. Hikita, J. Montoya, A. Doyle, C. Kirk, A. Vojvodic, H.Y. Hwang, J.K. Norskov, T.F. Jaramillo, A highly active and stable IrOx/SrIrO₃ catalyst for the oxygen evolution reaction, *Science* 353 (2016) 1011–1014.
- [2] H. Rao, L.C.S. Schmidt, J. Bonin, M. Robert, Visible-light-driven methane formation from CO₂ with a molecular iron catalyst, *Nature* 548 (2017) 74–77.
- [3] Q. Qian, Y. Li, Y. Liu, L. Yu, G. Zhang, Ambient fast synthesis and active sites deciphering of hierarchical foam-like trimetal-organic framework nanostructures as a platform for highly efficient oxygen evolution electrocatalysis, *Adv. Mater.* 31 (2019), 1901139.
- [4] X. Li, X. Huang, S. Xi, S. Miao, J. Ding, W. Cai, S. Liu, X. Yang, H. Yang, J. Gao, J. Wang, Y. Huang, T. Zhang, B. Liu, Single cobalt atoms anchored on porous N-Doped graphene with dual reaction sites for efficient Fenton-like catalysis, *J. Am. Chem. Soc.* 140 (2018) 12469–12475.
- [5] H. Zhao, C. Tian, J. Mei, S. Yang, P.K. Wong, Faster electron injection and higher interface reactivity in g-C₃N₄/Fe₂O₃ nanohybrid for efficient photo-Fenton-like activity toward antibiotics degradation, *Environ. Res.* 195 (2021), 110842.
- [6] J. Yan, J. Peng, L. Lai, F. Ji, Y. Zhang, B. Lai, Q. Chen, G. Yao, X. Chen, L. Song, Activation CuFe₂O₄ by hydroxylamine for oxidation of antibiotic sulfamethoxazole, *EST* 52 (2018) 14302–14310.
- [7] P. Chauhan, S. Chaudhary, One step production of Se doped carbon dots for rapid sensing of tetracycline in real water sample, *Opt. Mater.* 121 (2021), 111638.
- [8] T. Makropoulou, I. Kortidis, K. Davididou, D.E. Motaung, E. Chatzisyseon, Photocatalytic facile ZnO nanostructures for the elimination of the antibiotic sulfamethoxazole in water, *J. Water Process. Eng.* 36 (2020), 101299.
- [9] D.A. Nichela, J.A. Donadelli, B.F. Caram, M. Haddou, F.J.R. Nieto, E. Oliveros, F.S. G. Einschlag, Iron cycling during the autocatalytic decomposition of benzoic acid derivatives by Fenton-like and photo-Fenton techniques, *Appl. Catal. B* 170 (2015) 312–321.
- [10] J. Seo, S.Y. Park, J. Cho, J. Lee, H.-H. Kim, K.-M. Lee, A.L.T. Pham, C. Lee, Synergistic effects between the S-TiO₂ photocatalyst and the Fenton-like reagent: Enhanced contaminant oxidation under visible light illumination, *J. Environ. Chem. Eng.* 9 (2021), 104598.
- [11] J. Gao, S. Wu, Y. Han, F. Tan, Y. Shi, M. Liu, X. Li, 3D mesoporous CuFe₂O₄ as a catalyst for photo-Fenton removal of sulfonamide antibiotics at near neutral pH, *J. Colloid Interface Sci.* 524 (2018) 409–416.
- [12] S. Campos, R. Salazar, N. Arancibia-Miranda, M.A. Rubio, M. Aranda, A. Garcia, P. Sepulveda, L.C. Espinoza, Nafcillin degradation by heterogeneous electro-Fenton process using Fe, Cu and Fe/Cu nanoparticles, *Chemosphere* 247 (2020), 125813.
- [13] L. Hou, L. Wang, S. Royer, H. Zhang, Ultrasound-assisted heterogeneous Fenton-like degradation of tetracycline over a magnetite catalyst, *J. Hazard. Mater.* 302 (2016) 458–467.
- [14] A.G. Trovo, R.F.P. Nogueira, A. Agüera, A.R. Fernandez-Alba, S. Malato, Degradation of the antibiotic amoxicillin by photo-Fenton process-chemical and toxicological assessment, *Water Res.* 45 (2011) 1394–1402.
- [15] T.J. Al-Musawi, H. Kamani, E. Bazrafshan, A.H. Panahi, M.F. Silva, G. Abi, Optimization the effects of physicochemical parameters on the degradation of cephalixin in sono-Fenton reactor by using box-Behnken response surface methodology, *Catal. Lett.* 149 (2019) 1186–1196.

- [16] Q. Ouyang, F. Kou, N. Zhang, J. Lian, G. Tu, Z. Fang, Tea polyphenols promote Fenton-like reaction: pH self-driving chelation and reduction mechanism, *Chem. Eng. J.* 366 (2019) 514–522.
- [17] L. Hernández, P.A. Augusto, T. Castelo-Grande, D. Barbosa, Regeneration and reuse of magnetic particles for contaminant degradation in water, *J. Environ. Manag.* 285 (2021), 112155.
- [18] G. Subramanian, G. Madras, Remarkable enhancement of Fenton degradation at a wide pH range promoted by thioglycolic acid, *ChemComm* 53 (2017) 1136–1139.
- [19] Y. Zhang, R. Xiao, S. Wang, H. Zhu, H. Song, G. Chen, H. Lin, J. Zhang, J. Xiong, Oxygen vacancy enhancing Fenton-like catalytic oxidation of norfloxacin over prussian blue modified CeO_2 : Performance and mechanism, *J. Hazard. Mater.* 398 (2020), 122863.
- [20] W. Yang, P. Hong, D. Yang, Y. Yang, Z. Wu, C. Xie, J. He, K. Zhang, L. Kong, J. Liu, Enhanced Fenton-like degradation of sulfadiazine by single atom iron materials fixed on nitrogen-doped porous carbon, *J. Colloid Interface Sci.* 597 (2021) 56–65.
- [21] L. Li, C. Hu, L. Zhang, G. Yu, L. Lyu, F. Li, N. Jiang, Framework Cu-doped boron nitride nanobelts with enhanced internal electric field for effective Fenton-like removal of organic pollutants, *J. Mater. Chem. A* 7 (2019) 6946–6956.
- [22] M.A. Younis, S. Lyu, C. Lei, B. Yang, Z. Li, Q. He, J. Lu, L. Lei, Y. Hou, Efficient mineralization of sulfanilamide over oxygen vacancy-rich NiFe-LDH nanosheets array during electro-fenton process, *Chemosphere* 268 (2021), 129272.
- [23] Z. Xie, J. Zhou, J. Wang, C.P. François-Xavier, T. Wintgens, Novel Fenton-like catalyst $\gamma\text{-Cu-Al}_2\text{O}_3\text{-Bi}_2\text{O}_3\text{-Cl}_6$ with electron-poor Cu centre and electron-rich Bi centre for enhancement of phenolic compounds degradation and H_2O_2 utilization: The synergistic effects of $\sigma\text{-Cu-ligand}$, dual-reaction centres and oxygen vacancies, *Appl. Catal. B* 253 (2019) 28–40.
- [24] Y. Zhuang, Q.Z. Liu, Y. Kong, C.C. Shen, H.T. Hao, D.D. Dionysiou, B.Y. Shi, Enhanced antibiotic removal through a dual-reaction-center Fenton-like process in 3D graphene based hydrogels, *Environ. Sci. Nano* 6 (2019) 388–398.
- [25] M.K. Panjwani, Q. Wang, Y. Ma, Y. Lin, F. Xiao, S. Yang, High degradation efficiency of sulfamethazine with the dual-reaction-center Fe-Mn-SiO₂ Fenton-like nanocatalyst in a wide pH range, *Environ. Sci. Nano* 8 (2021) 2204–2213.
- [26] S. Xu, H. Zhu, W. Cao, Z. Wen, J. Wang, C.P. François-Xavier, T. Wintgens, $\text{Cu-Al}_2\text{O}_3\text{-g-C}_3\text{N}_4$ and $\text{Cu-Al}_2\text{O}_3\text{-C-dots}$ with dual-reaction centres for simultaneous enhancement of Fenton-like catalytic activity and selective H_2O_2 conversion to hydroxyl radicals, *Appl. Catal. B* 234 (2018) 223–233.
- [27] X. Zhang, Z.P. Yao, Y. Zhou, Z.R. Zhang, G.F. Lu, Z.H. Jiang, Theoretical guidance for the construction of electron-rich reaction microcenters on C-O-Fe bridges for enhanced Fenton-like degradation of tetracycline hydrochloride, *Chem. Eng. J.* 411 (2021), 128535.
- [28] N. Wang, W. Ma, Z. Ren, L. Zhang, R. Qiang, K.Y.A. Lin, P. Xu, Y. Du, X. Han, Template synthesis of nitrogen-doped carbon nanocages-encapsulated carbon nanobubbles as catalyst for activation of peroxymonosulfate, *Inorg. Chem. Front.* 5 (2018) 1849–1860.
- [29] S.H. Ho, Y.D. Chen, R.X. Li, C.F. Zhang, Y.M. Ge, G.L. Cao, M. Ma, X.G. Duan, S. B. Wang, N.Q. Ren, N-doped graphitic biochars from C-phycocyanin extracted Spirulina residue for catalytic persulfate activation toward nonradical disinfection and organic oxidation, *Water Res.* 159 (2019) 77–86.
- [30] Y. Fujimoto, S. Saito, Structure and stability of hydrogen atom adsorbed on nitrogen-doped carbon nanotubes, *J. Phys.: Conf. Ser.* 302 (2011), 012006.
- [31] G. Kresse, J. Hafner, Ab initio molecular dynamics for liquid metals, *Phys. Rev. B* 47 (1993) 558–561.
- [32] G. Kresse, J. Furthmüller, Efficient iterative schemes for ab initio total-energy calculations using a plane-wave basis set, *Phys. Rev. B* 54 (1996) 11169–11186.
- [33] G. Kresse, D. Joubert, From ultrasoft pseudopotentials to the projector augmented-wave method, *Phys. Rev. B* 59 (1999) 1758–1775.
- [34] P.E. Blochl, Projector augmented-wave method, *Phys. Rev. B* 50 (1994) 17953–17979.
- [35] J.P. Perdew, K. Burke, M. Ernzerhof, Generalized gradient approximation made simple, *Phys. Rev. Lett.* 77 (1996) 3865–3868.
- [36] H.J. Monkhorst, J.D. Pack, Special points for Brillouin-zone integrations, *Phys. Rev. B: Condens. Matter* 13 (1976) 5188–5192.
- [37] S. Grimme, J. Antony, S. Ehrlich, H. Krieg, A consistent and accurate ab initio parametrization of density functional dispersion correction (DFT-D) for the 94 elements H-Pu, *J. Chem. Phys.* 132 (2010), 154104.
- [38] H. Wang, F. Meng, J. Li, T. Li, Z. Chen, H. Luo, Z. Zhou, Carbonized design of hierarchical porous carbon/ Fe_3O_4 @Fe derived from loofah sponge to achieve tunable high-performance microwave absorption, *ACS Sustain. Chem. Eng.* 6 (2018) 11801–11810.
- [39] V.O.A. Tanobe, T.H.D. Sydenstricker, M. Munaro, S.C. Amico, A comprehensive characterization of chemically treated Brazilian sponge-gourds (*Luffa cylindrica*), *Polym. Test.* 24 (2005) 474–482.
- [40] C. Mancera, F. Ferrando, J. Salvado, N.E. El Mansouri, Kraft lignin behavior during reaction in an alkaline medium, *Biomass-Bioenerg.* 35 (2011) 2072–2079.
- [41] X.J. Hou, X.P. Huang, Z.H. Ai, J.C. Zhao, L.Z. Zhang, Ascorbic acid/ $\text{Fe}@\text{Fe}_2\text{O}_3$: a highly efficient combined Fenton reagent to remove organic contaminants, *J. Hazard. Mater.* 310 (2016) 170–178.
- [42] N. Jiang, L. Lyu, G. Yu, L. Zhang, C. Hu, A dual-reaction-center Fenton-like process on $\text{—C}\equiv\text{N—Cu}$ linkage between copper oxides and defect-containing $\text{g-C}_3\text{N}_4$ for efficient removal of organic pollutants, *J. Mater. Chem. A* 6 (2018) 17819–17828.
- [43] C. Janiak, A critical account on pi-pi stacking in metal complexes with aromatic nitrogen-containing ligands, *J. Chem. Soc. Dalton Trans.* (2000) 3885–3896.
- [44] Z. Xu, Y. Du, D. Liu, Y. Wang, W. Ma, Y. Wang, P. Xu, X. Han, Pea-like $\text{Fe}/\text{Fe}_3\text{C}$ nanoparticles embedded in nitrogen-doped carbon nanotubes with tunable dielectric/magnetic loss and efficient electromagnetic absorption, *ACS Appl. Mater. Inter.* 11 (2019) 4268–4277.
- [45] N. Wang, W. Ma, Z. Ren, Y. Du, P. Xu, X. Han, Prussian blue analogues derived porous nitrogen-doped carbon microspheres as high-performance metal-free peroxymonosulfate activators for non-radical-dominated degradation of organic pollutants, *J. Mater. Chem. A* 6 (2018) 884–895.
- [46] G. Zhong, H. Wang, H. Yu, F. Peng, Nitrogen doped carbon nanotubes with encapsulated ferric carbide as excellent electrocatalyst for oxygen reduction reaction in acid and alkaline media, *J. Power Sources* 286 (2015) 495–503.
- [47] A. Wu, D. Liu, L. Tong, L. Yu, H. Yang, Magnetic properties of nanocrystalline $\text{Fe}/\text{Fe}_3\text{C}$ composites, *Crystengcomm* 13 (2011) 876–882.
- [48] V.V. Kovalevski, A.N. Safronov, Pyrolysis of hollow carbons on melted catalyst, *Carbon* 36 (1998) 963–968.
- [49] Z. Liu, X. Zhang, Z. Jiang, P. Yang, G. Gao, N-doped bamboo-like carbon nanotubes loading Co as ideal electrode material towards superior catalysis performance, *Int. J. Hydrog. Energy* 45 (2020) 8703–8714.
- [50] T. Ouyang, Y. Ye, C. Wu, K. Xiao, Z. Liu, Heterostructures composed of N-doped carbon nanotubes encapsulating cobalt and beta- Mo_2C nanoparticles as bifunctional electrodes for water splitting, *Angew. Chem. Int. Ed.* 58 (2019) 4923–4928.
- [51] B. Cai, J.F. Feng, Q.Y. Peng, H.F. Zhao, Y.C. Miao, H. Pan, Super-fast degradation of high concentration methyl orange over bifunctional catalyst $\text{Fe}/\text{Fe}_3\text{C}@C$ with microwave irradiation, *J. Hazard. Mater.* 392 (2020), 122279.
- [52] S. Wu, H. Liu, C. Yang, X. Li, Y. Lin, K. Yin, J. Sun, Q. Teng, C. Du, Y. Zhong, High-performance porous carbon catalysts doped by iron and nitrogen for degradation of bisphenol F via peroxymonosulfate activation, *Chem. Eng. J.* 392 (2020), 123683.
- [53] X. Li, Y. Jia, M. Zhou, X. Su, J. Sun, High-efficiency degradation of organic pollutants with Fe, N co-doped biochar catalysts via persulfate activation, *J. Hazard. Mater.* 397 (2020), 122764.
- [54] W. Weng, J. Zhou, D. Gu, W. Xiao, Thermoelectrochemical formation of $\text{Fe}/\text{Fe}_3\text{C}@$ hollow N-doped carbon in molten salts for enhanced catalysis, *J. Mater. Chem. A* 8 (2020) 4800–4806.
- [55] K. Kohila Rani, C. Karupiah, S.F. Wang, S.O. Alaswad, P. Sireesha, R. Devasenathipathy, R. Jose, C.C. Yang, Direct pyrolysis and ultrasound assisted preparation of N co-doped graphene/ Fe_3C nanocomposite as an efficient electrocatalyst for oxygen reduction and oxygen evolution reactions, *Ultrason. Sonochem.* 66 (2020), 105111.
- [56] Y. Li, W. Ma, J. Sun, M. Lin, Y. Niu, X. Yang, Y. Xu, Electrochemical generation of $\text{Fe}_3\text{C}/\text{N}$ -doped graphitic carbon nanozyme for efficient wound healing in vivo, *Carbon* 159 (2020) 149–160.
- [57] K. Zhu, Q. Bin, Y. Shen, J. Huang, D. He, W. Chen, In-situ formed N-doped bamboo-like carbon nanotubes encapsulated with Fe nanoparticles supported by biochar as highly efficient catalyst for activation of persulfate (PS) toward degradation of organic pollutants, *Chem. Eng. J.* 402 (2020), 126090.
- [58] J. Shi, Y. Wang, W. Du, Z. Hou, Synthesis of graphene encapsulated Fe_3C in carbon nanotubes from biomass and its catalysis application, *Carbon* 99 (2016) 330–337.
- [59] Y. Ma, A. Song, S. Yan, H. He, G. Shao, Direct solid-state growth of Fe/N co-doped coordination structure between carbon nanotubes and ultra-thin porous carbon nanosheets towards oxygen reduction reaction, *Electrochim. Acta* 353 (2020), 136568.
- [60] X. Yang, X. Sun, M. Rauf, H. Mi, L. Sun, L. Deng, X. Ren, P. Zhang, Y. Li, N-doped porous tremella-like $\text{Fe}_3\text{C}/\text{C}$ electrocatalysts derived from metal-organic frameworks for oxygen reduction reaction, *Dalton Trans.* 49 (2020) 797–807.
- [61] O.B. Popovicheva, E.D. Kireeva, N.K. Shonija, M. Vojtisek-Lom, J. Schwarz, FTIR analysis of surface functionalities on particulate matter produced by off-road diesel engines operating on diesel and biofuel, *Environ. Sci. Pollut. Res.* 22 (2015) 4534–4544.
- [62] B.R. Ganapuram, M. Alle, R. Dadigala, A. Dasari, V. Maragoni, V. Guttena, Catalytic reduction of methylene blue and Congo red dyes using green synthesized gold nanoparticles capped by salmali malabarica gum, *Int. Nano Lett.* 5 (2015) 215–222.
- [63] A.H. Cahyana, B. Ardiansah, A. Nadila, Functionalization of cinnamaldehyde to arylidene barbituric acid catalyzed by samarium (III) chloride, *Orient. J. Chem.* 34 (2018) 2685–2688.
- [64] G. Kandhol, H. Wadhwa, S. Chand, S. Mahendia, S. Kumar, Study of dielectric relaxation behavior of composites of Poly (vinyl alcohol)(PVA) and reduced graphene oxide (RGO), *Vacuum* 160 (2019) 384–393.
- [65] Q. Pan, Q. Gao, G. Gao, M. Liu, B. Han, K. Xia, C. Zhou, Composition-engineered LaCoO_3 -based monolithic catalysts for easily operational and robust peroxymonosulfate activation, *Chem. Eng. J.* 424 (2021), 130574.
- [66] J.F. Zang, C.M. Li, X.Q. Cui, J.X. Wang, X.W. Sun, H. Dong, C.Q. Sun, Tailoring zinc oxide nanowires for high performance amperometric glucose sensor, *Electroanalysis* 19 (2007) 1008–1014.
- [67] S. Srinivasan, P. Athappan, G. Rajagopal, Synthesis, spectral and redox properties of metal complexes of macrocyclic tetraaza chiral Schiff bases, *Transit. Met. Chem.* 26 (2001) 588–593.
- [68] Z. Ai, Z. Gao, L. Zhang, W. He, J.J. Yin, Core-shell structure dependent reactivity of $\text{Fe}@\text{Fe}_2\text{O}_3$ nanowires on aerobic degradation of 4-chlorophenol, *EST* 47 (2013) 5344–5352.